J Mater Sci: Mater Med (2011) 22:1321–1332
DOI 10.1007/s10856-011-4309-4

Direct visualization and quantification of bone growth into porous titanium implants using micro computed tomography

E. Baril · L. P. Lefebvre · S. A. Hacking

Received: 17 December 2010 / Accepted: 25 March 2011 / Published online: 22 April 2011

Abstract The utility of porous metals for the integration of orthopaedic implants with host bone has been well established. Quantification of the tissue response to cementless implants is laborious and time consuming process requiring tissue processing, embedding, sectioning, polishing, imaging and image analysis. Micro-computed tomography (μCT) is a promising three dimensional (3D) imaging technique to quantify the tissue response to porous metals. However, the suitability and effectiveness of μCT for the quantification of bone ingrowth remains unknown. The purpose of this study was to evaluate and compare bone growth within porous titanium implants using both μCT and traditional hard-tissue histology techniques. Cylindrical implants were implanted in the distal femora and proximal tibiae of a rabbit. After 6 weeks, bone ingrowth was quantified and compared by μCT, light microscopy and backscattered electron microscopy. Quantification of bone volume and implant porosity as determined by μCT compared well with data obtained by traditional histology techniques. Analysis of the 3D dataset showed that bone was present in the pores connected with openings larger 9.4 μm. For pore openings greater than 28.2 μm, the size of the interconnection had little impact on the bone density within the porosity for the titanium foams.

E. Baril (✉) · L. P. Lefebvre
National Research Council Canada—Industrial Materials Institute, 75 de Mortagne Blvd., Boucherville, QC J4B 6Y4, Canada
e-mail: eric.baril@cnrc-nrc.gc.ca

S. A. Hacking
Harvard Medical School and Massachusetts General Hospital - Department of Orthopedics, 55 Fruit St, GRJ 1120, Boston, MA 02114, USA

1 Introduction

Orthopedic devices with porous coatings have been used for three decades as a means to achieve fixation by integration with osseous tissue (osseointegration). The majority of porous metal coatings are produced by sintering titanium beads, mesh or fibers or by plasma spraying of titanium particulates. Under appropriate conditions, the growth of bone into the porosity of these coatings results in long-term mechanical fixation of the implanted device to the host skeleton. The success of implant fixation by osseointegration has been well established for many reconstructive procedures [1, 2]. Recent advances in materials and manufacturing methods have enabled the fabrication of entirely porous metal implants for skeletal repair [3–5]. These new materials, as opposed to sintered beads or mesh coatings, have larger porosity and provide better friction with bone [6, 7]. These characteristics may enable increased bone ingress resulting in a stronger bone-implant interface which in turn may facilitate the development of improved treatments for musculoskeletal repair and reconstruction.

The development and validation of new materials for implant fixation is a major effort requiring quantification of the rate, extent, and amount of bone ingrowth. Conventional histological or metallographic two-dimensional (2D) sectioning techniques have been used predominantly to quantify bone growth into porous coatings using light microscopy (LM) and/or backscattered scanning electron microscopy (BSEM) [8]. Post-processing of acquired images routinely includes digital image analysis to determine the porosity, pore size and ratio of bone area to porous area (% ingrowth) [9]. While standard 2D histology techniques are effective, sample preparation is laborious, time consuming and results in the destruction of the

specimen. Other drawbacks of sectioning techniques include the sampling of a limited subset of the entire specimen and the inability to efficiently provide detailed information regarding a variety of three dimensional (3D) spatial parameters such as the effect of connectivity on bone ingrowth [10]. High resolution, 3D imaging techniques such as micro computed tomography (μCT) have been advantageous for analysis of bone morphology when compared to conventional 2D techniques [10–12]. The advantages of μCT are the ability to provide quantitative results without destroying the sample, there is little sample preparation, the entire sample is analysed and the tissue response to the sample can be viewed in many planes. μCT also permits the direct measurement of pore morphology, size distribution and connectivity.

As an analytical technique, μCT has been used to quantify and characterize changes in bone architecture associated with bone disorders such as osteoporosis [13–16]. μCT has also been used to quantify the bone contact area (apposition) between a solid non-porous implant and adjacent bone [17]. It is important to note however, that the application of μCT to quantify bone growth *within* porous metal implants is *markedly different* from quantification of bone contact to a solid (non porous) implant surface. Technical challenges include the difficulty of differentiating the bone and metal phases at scales approaching the resolution of most current μCT equipments. This represents a significant problem for metallic foams as the pore diameters are typically between 50 and 400 μm [18]. Reconstructed volumes are also affected by different hardware-related imaging artefacts, such as beam hardening from *polychromatic* X-ray sources and the reminiscence of the detector, which may impair the visualization of bone within distance up to 200 μm from the metal surface [17, 19].

Not surprisingly, there are few examples in the literature demonstrating the use of μCT to assess bone formation within porous implants and most work indirectly measures bone response. For example, Otsuki et al. [20] showed a correlation between pore connectivity and bone formation by comparing histology sections (tissue response) to 2D images of the implant architecture obtained by μCT prior to implantation. Jones et al. [21] demonstrated the effect of pore connectivity on bone growth into porous hydroxyapatite (Hap) and alumina scaffolds. They underlined the difficulties associated with phase separation in these multiphase specimens (scaffold, mineralized matrix, non-mineralized tissues and embedding media) and presented a three-phase segmentation technique to enable the separation of the scaffold and mineralized bone. The resulting datasets were used to visualize bone ingrowth in 3D and to quantify bone density by image analysis. However, the implants characterized contained only a few pores.

While technically challenging, there are many obvious benefits for the direct quantification of bone growth into porous metal implants using μCT and 3D image analysis. However, from a practical and quantitative perspective, the effectiveness of μCT remains unknown since a direct comparison to traditional analytical methods has not been performed. As a result, the aims of this study were: (1) to determine optimal analytical parameters such as μCT operating conditions and image analysis procedures, (2) to determine if μCT was a suitable tool for the visualisation and quantification of bone growth into porous Ti foam implants and (3) to characterize bone ingrowth using μCT and 3D image analysis.

2 Materials and methods

2.1 Implant preparation and characterization

Cylindrical implants, 4 mm in diameter and 5 mm in length, were prepared using a Ti foam process [22–24] (Fig. 1). Briefly, a commercially pure titanium powder (CpTi—Grade 1, Advanced Powders and Coatings, Boisbriand, QC) was admixed with a binder and a chemical foaming agent. The resulting powder mixture was poured into a cylindrical mold and heated to foam the material. During the foaming treatment, the binder melted and formed a suspension with the Ti particles while the decomposition of the foaming agent generated a gas that expanded (foamed) the suspension. The resulting material (polymer foam charged with the Ti particles) was then successively debinded and sintered under vacuum to consolidate the material.

The implant porosity was determined by three methods. The first method uses the overall implant density, calculated by measuring the implant weight and dimensions, which is then compared to the CpTi density as determined on the starting powder using a Helium gas pycnometer (Micromeritics, Norcross, GA). The method is referred to below as geometric density. In the second method, the volume of Ti was determined by Ti phase segmentation of the μCT volume. The third method used the Ti foam fractional surface area measured from image analysis of 2D sections (BSEM and μCT).

Prior to implantation, CpTi implants were cleaned by sonication for 30 min in a 1% (v/v) detergent solution of Liquinox (Liquinox, White Plains, NY) and distilled water (dH_2O) then rinsed 3 times in dH_2O. Following cleaning, the Ti implants were passivated for 30 min in a 35% (v/v) solution of nitric acid (Fisher Scientific, Ottawa, ON) then rinsed 3 times in dH_2O. Implants were double packaged in sterilizable pouches (Crosstex, Hauppauge, NY) and steam sterilized at 135°C for 20 min.

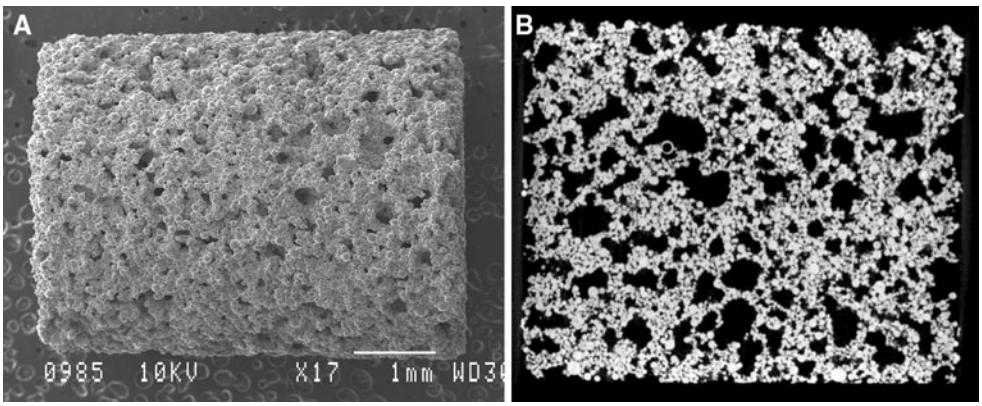

Fig. 1 **a** Low power scanning electron microscopy (SEM) image of the titanium foam implant. **b** 2D cross section of the implant obtained by μCT showing the porosity produced during the foaming process. Implant porosity is highly dependent upon the foaming process and not the bead diameter

2.2 Surgical procedure

Using standard aseptic techniques, one male New Zealand white rabbit (4 kg) underwent bilateral surgery and received a total of 8 porous Ti implants in the cancellous bone beds of the distal femur and proximal tibia. Each femur received 2 implants placed in the medial and lateral condyles and each tibia received 2 implants placed anteriorly just below the tibial tuberosity. A longitudinal incision centered over the knee and extending 4 cm exposed the proximal anterior surface of the rabbit tibia and permitted access to the femoral condyles. The periosteum was carefully elevated and retracted from the underlying cortical bone. Using constant irrigation, a 3.9 mm hole was drilled for each implant (0.05 mm press fit) and implants were gently tapped into position. The periosteum was re-approximated and tissue layers closed with 4–0 resorbable sutures. Post-operatively, the animal received cephazolin (7.5 mg/kg BID) and buprenorphine (0.05 mg/kg TID) for 5 days. All procedures were performed in accordance with the policy on animal use of McGill University.

2.3 Specimen preparation and histologic analysis

After 6 weeks, the implants were retrieved within the surrounding bone and high resolution digital radiographs (Faxitron, Wheeling, IL) of the implants in situ were obtained for later comparison to 3D reconstructions. Specimens were fixed in a 4% solution of para-formaldehyde, dehydrated in ascending solutions of ethanol, defatted in a 1:1 mixture of ether:acetone followed by immersion in 100% ethanol prior to infiltrating and embedding in methyl methacrylate [25]. Prior to sectioning, implants were scanned by μCT as described below. Following scanning, the specimens were processed for histologic analysis by sectioning longitudinally using a diamond saw (Buehler, Markham ON). Sectioning of each implant produced two blocks, exposing the central portion of the implant in each. Sections were then sputter coated with Au/Pd and analyzed by backscattered scanning electron microscopy (BSEM) (JEOL, Peabody, MA) to visualize bone within the implant [26]. Following BSEM imaging, the sputter coated Au/Pd layer was removed by wiping with 95% ethanol. Each half of the implant was sectioned (again) parallel to and just beneath the original bisection, with a Leica SP-1600 diamond saw (Richmond Hill, Ontario) to produce thin, sub-100 μm sections suitable for light microscopy (LM). LM sections were stained with basic fuchsin and methylene blue to enable visualization of both mineralized and soft tissues [27].

2.4 Micro computed tomography image acquisition and reconstruction

Prior to sectioning, intact, embedded implants were scanned by μCT and quantified using 3D analysis. A general scan was obtained to locate and visualize the implant in the distal femur. Extraneous material was removed using a precision sectioning diamond saw to enhance scan resolution. After sectioning, the specimens prepared for LM and BSEM were scanned again using μCT. This was done to compare the quality of the μCT images directly with images obtained by standard histologic techniques.

The μCT scans were obtained using an X-Tek HMXST 225 microfocus X-ray system (Nikon Metrology, Tring, UK). The spot size of the X-ray source was estimated between 4.5 and 7.5 μm, using standard TEM nickel grids (SPI supplies, West Chester, PA), for the conditions used in this study (see Table 1). A 0.5 mm Cu filter was used at the source to reduce beam hardening effects. The cone beam produced from the polychromatic microfocus source was detected using a PE 1621 AN amorphous silicon

Table 1 Acquisition conditions and parameters of the μCT reconstructed volumes from the specimen scanned in this study

Specimen scanned by μCT	Specimen size (mm)	X-ray source voltage (kV)	X-ray source current (uA)	Source to specimen distance (mm)	Angle increments between projections (°)	X-ray panel parameters Integration time Number of averaged frames	Voxel size (μm)	Image size (voxel)
Ti-Foam cylinder	4.8 dia. 6.1 length	130	69	21.4694	0.1162	708 ms 8 frames	4.9	*x*:988 *y*:946 *z*:1251
Ti-Foam implant in condyles of the distal femur	*x*:22.1 *y*:19.5 *z*:22.5	70	702	106.2655	0.18	250 ms 1 frame	18.1	*x*:1221 *y*:1076 *z*:1245
Zoom on Ti-Foam implant in condyles of distal femur	*x*:6.0 *y*:5.9 *z*:5.9	120	79	34.0505	0.1419	500 ms 8 frames	4.7	*x*:1273 *y*:1254 *z*:1262
BSEM sample	*x*:1.8 *y*:6.1 *z*:5.9	110	59	30.1329	0.1902	1000 ms 16 frames	3.7	*x*:476 *y*:1660 *z*:1590
LM sample	*x*:0.8 *y*:5.9 *z*:6.3	105	69	28.3151	0.1975	1000 ms 16 frames	3.4	*x*:244 *y*:1732 *z*:1866

409.6 × 409.6 mm flat panel detector coupled with a CsI scintillator screen (PerkinElmer Optoelectronics, Fremont, CA) located at 1173 mm from the X-ray source. For a full 360° rotation of the specimen, 16-bit grey-scale images of 2000 × 2000 pixels (radiographic projection) were obtained for each rotation increment. For each projection, random displacement of the specimen rotation axis along the axis parallel to the detector plane was used to eliminate ring artefacts. The 3D cone beam reconstructions were performed using X-Tek CT-Pro software based on Feldkamp-Davis-Kress (FDK) algorithm [28]. The cubic voxel size was affected by the position of the specimen between the source and the detector. This distance was affected by the size of the specimens. The files generated were typically between 4 and 8 Gigabytes. The acquisition conditions and the parameters of the reconstructed volumes are presented in Table 1.

2.5 Histomorphometric evaluation

ORS Visual (Objects Research Systems, Montreal, Canada) was used for the 3D analysis of the μCT images. Figure 2 presents the workflow diagram while Fig. 3 provides key images during processing. The original image (Fig. 3a) was first treated using a 3D median filter using a 5 voxels diameter spherical kernel in order to remove noise while maintaining sharp interfaces between the mineralized matrix and the Ti phase. The image was then clipped electronically to treat the intra-implant (including the bone inside the porosity) separately from the peri-implant bone. Segmentation (phase separation) was then applied on each area (inside and outside the implant) separately. The threshold value for each area was determined by comparing 2D sections from the original and segmented images for all μCT scans [12]. The threshold was optimized to fully select the phase of interest with minimal oversampling of other phases. This optimization was performed to retain bone found within the pores while reducing the thickness of the 'shell' artifact surrounding the titanium phase to 3–8 voxels (see Fig. 3f). The local threshold method minimized measurement artifacts due to the detector reminiscence which increases the grey level value of the phases in the pores when compared to the same phases outside the implant. This method also enhances accurate representation of the mineralized matrix inside and outside the foam. Figure 3b and d present the image after segmentation of the mineralized matrix (red) outside and inside the implant respectively. The binary image of the segmented mineralized matrix inside the foam was further treated by 2 cycles of 3D morphological opening using a 5 voxels diameter spherical kernel. This operation removed the 'shells' surrounding the Ti phase resulting from the blurring of the bone-Ti interface due to the spatial resolution of the technique (see Fig. 3f, g). Such operation removes features 8 voxels in one direction or less, which is equivalent to 37.6 μm. Finally, the two sections were merged together to reconstruct the complete image (implant and bone ingrown + adjacent, external bone). The final image

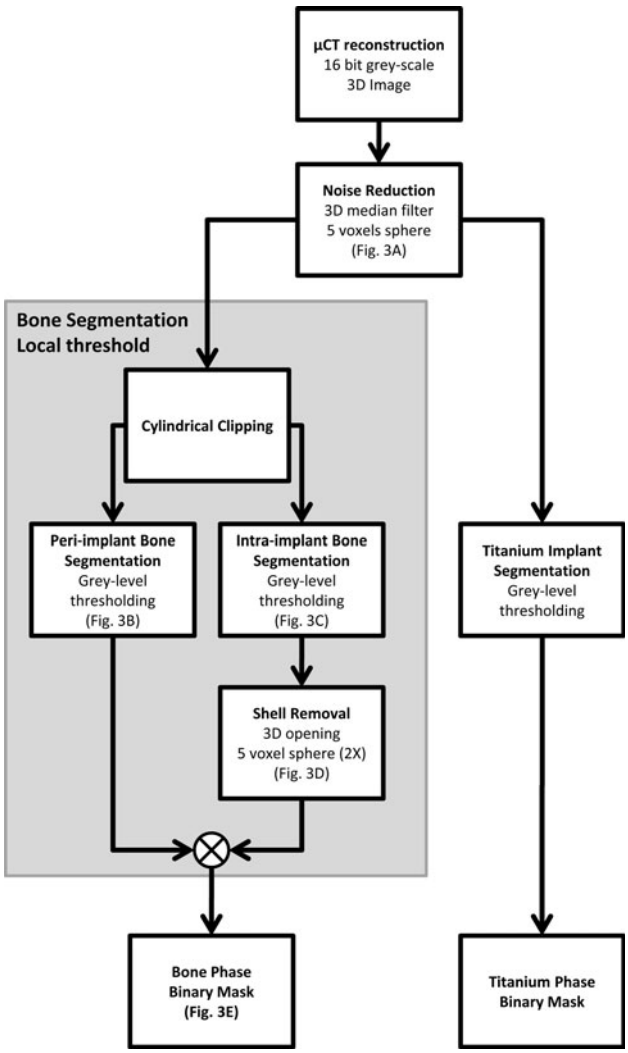

Fig. 2 Phase segmentation workflow diagram

(Fig. 3e) corresponds well with the initial image (Fig. 3a) and shows that the segmentation and treatment of the images enhanced significantly the visibility of the information available in the initial image. Bone connectivity was determined using a connected threshold growing filter which label voxels that are connected to a seed and lie within a range of grey values. This range was determined using the average and standard deviation within a 5 voxels diameter spherical seed point. Bone paths along the porous network were visualized using a "fastmarching" front that propagates from selected points in the bone structure outside of the implant to all the connected bone points [29]. A speed map (i.e. gradient descent algorithm on the "fastmarching" result) was used to locate all the continuous paths connected to source points. An unwrapping algorithm was used to visualize in 2D continuous bone segments inside the porous network. To study the impact of the porous network interconnectivity on bone ingrowth, successive morphological dilations using a 4.7 µm voxel kernel on the segmented Ti foam volume was used to gradually close the pore interconnections. The mineralized bone matrix volume fraction in pores closed by a given level of dilation was then calculated. This operation was performed on the entire volume of the implant to evaluate the effect pore interconnection size on bone ingrowth.

3 Results

3.1 Implant porosity and pore size measured before implantation

Finding the appropriate threshold represents an inherent difficulty in the segmentation of a large dynamic range images such as those obtained with µCT and BSEM. In this study, the µCT 3D dataset was segmented using a threshold value calibrated on one specific specimen using the porosity measurement obtained by measuring geometric density. This threshold value was subsequently used for analysis of all specimens in both 3D and 2D. As a result, implant porosity determined by µCT (51.6%) was not significantly different than the porosity obtained using geometric measurements (53.1%) (Table 2). The µCT and segmentation techniques allowed accurate quantification of the implant porosity with a standard deviation close to that calculated using geometric density.

The porosity measured in 2D on BSEM images and 2D sections generated from µCT reconstructions (Table 3) can be compared with those obtained by 3D analysis of the entire specimen (Table 2). The average porosity measured in 2D with µCT (48.4 ± 0.6%) was similar to that obtained in 3D (51.6 ± 1.2%). The porosity determined using the 2D BSEM cross sections (44.0 ± 2.3%) was significantly lower than the porosity measured geometrically (53.1 ± 1.8%).

The average pore size determined from the 2D µCT images (375 ± 61 µm) was slightly larger but not statistically different from that obtained from the BSEM sections (333 ± 29 µm). The effect of spatial resolution, image pixel size and segmentation of the different techniques did not have an important impact on the evaluation of the average pore size, at least for the conditions used in this study.

3.2 Analysis of implant osseointegration

There were no surgical or post-operative complications, indications of infection or abnormal tissue response at the time of retrieval. High-resolution radiographs of the implants *in situ* were obtained immediately after retrieval and all implants appeared to be stable with no peri-implant

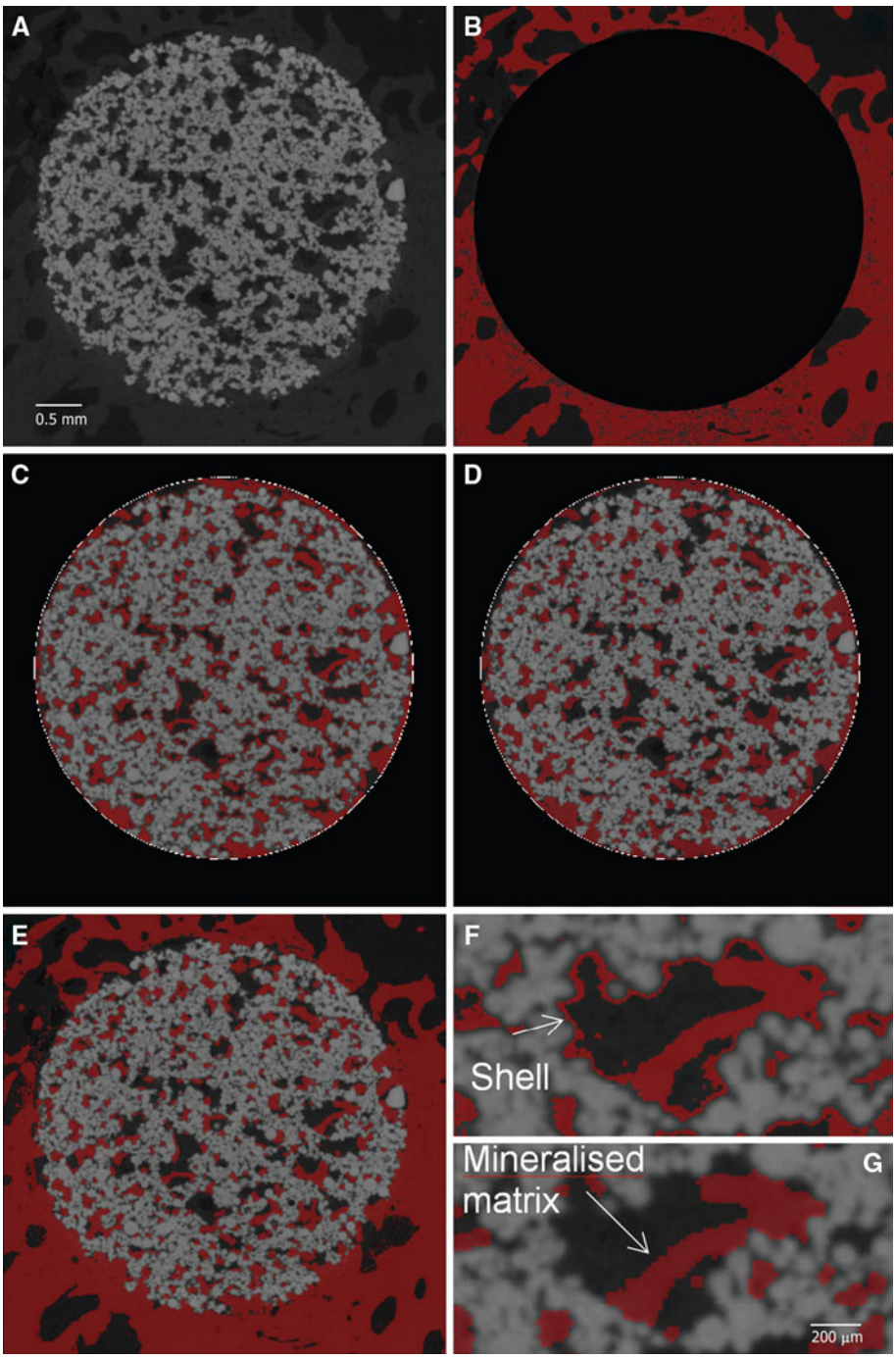

Fig. 3 Image processing sequence on a 2D cross section obtained from a µCT image (4.7 µm voxel size) **a** original image, **b** sectioning of the image to adjust separately the segmentation of the bone mineralized matrix outside of the implant, **c** segmentation of the bone mineralized matrix optimized for the bone inside the implant; **d** 2 cycles of 3D morphological opening to remove the presence of *shells* (imaging artifacts) around the titanium phase. **e** Merging of the 2 images (**b**) and (**d**) to obtain the image of the titanium phase in *grey* with the segmented bone mineralized matrix in *red*. **f** Higher magnification image showing the results of segmentation of the mineralized matrix (*red*); **g** same image after 2 cycles of 3D morphological dilation and erosion to remove bone-like artifacts (*shell*) around the titanium phase. **b–g** Implant is *grey* and bone is *red*. Scale **a–e** = 0.5 mm and **e–f** = 200 µm (Color figure online)

Table 2 Average porosity determined by geometric measurements and by image analysis from µCT 3D reconstructions

Analysis technique	Avg. porosity (%)
Geometric ($n = 48$)	53.1 ± 1.8
µCT (3D) ($n = 3$)	51.6 ± 1.2

Table 3 Average porosity and average pore size evaluated in 2D from BSEM and µCT 2D cross-sections

Analysis technique	Avg. porosity (%)	Avg. pore size (µm)
BSEM (2D)	44.0 ± 2.3 ($n = 8$)	333.0 ± 29 ($n = 8$)
µCT (2D)	48.4 ± 0.6 ($n = 3$)	375.3 ± 61 ($n = 3$)

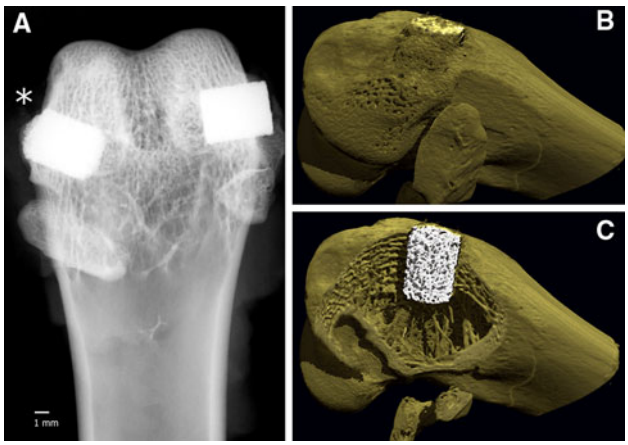

Fig. 4 **a** High resolution radiographs of the cylindrical porous titanium implants in the condyles of the distal femur after 6 weeks in situ. **b** Micro computed tomography 3D reconstruction of one of the implants from **a** (*asterisk*) in the condyle of the distal femur (implant *white*, bone *brown*). **c** 3D visualization of the implant in situ. Part of the bone has been digitally removed to illustrate the trabecular architecture surrounding the implant. Compared to 2D radiographs, 3D reconstructions provide enhanced information regarding implant position and architecture of the surrounding osseous tissue (Color figure online)

defects or radiolucent regions (Fig. 4). 3D visualization of the implant in situ by μCT provided enhanced information regarding implant position and architecture of the surrounding osseous tissue. The 3D reconstructions showed that the implant was well integrated in the bone structure with new bone formation surrounding the implant.

3.3 Comparison of imaging techniques

Figure 5 compares BSEM and μCT images of a longitudinal section cut from a retrieved and osseointegrated porous Ti implant. In all images, the Ti scaffold (white) and the mineralized matrix (grey) are clearly visible. New bone spanned the diameter of the implant from cortex to cortex and regions of new bone were observed within the implant. The Ti phase and bone correspond well on the images taken with both techniques. When qualitatively compared, the sharpness and the contrast of the BSEM images were superior to the μCT images. However, these differences in qualitative appearance had no significant effect on quantitative analysis (Fig. 5) as the resolutions of the images for both techniques were similar (around 5–7 μm). It should be noted that low density materials such as non-mineralized tissues and mounting media cannot be differentiated using both techniques and appear as black regions in the images.

A direct comparison between the μCT and LM images was performed on a histology section prepared for optical microscopy (Fig. 6). In the LM image (Fig. 6a), the Ti scaffold is black, bone is stained red, non-mineralized tissues are blue and the embedding material is not visible (i.e. clear). In the original μCT images (Fig. 6b, c), the Ti is white and the mineralized matrix is grey (red after segmentation). Qualitatively, both imaging methods produced very similar representations of the scaffold and bone tissue. An obvious difference of the LM preparation was the ability to visualize non-mineralized tissues. Significant differences were observed between the porosities measured by image analysis from the LM images and those obtained using geometrical measurements or image analysis from 3D μCT reconstructions (22% vs. 51.6 ± 1.2%; Table 2). Small and insignificant differences were also observed in the average pore size when comparing the values obtained in 2D on the μCT cross sections with those obtained on the BSEM images (333 ± 29 vs. 375.3 ± 61 μm, respectively).

Bone formation, porosity and pore size within the implant could be visualized and assessed in any plane by μCT whereas BSEM and LM enabled visualization only in the plane that the implant was sectioned. The ability to section, visualize and quantify bone within discrete sections from the implant is shown in Fig. 7. By virtually sectioning the implant, differences in bone ingrowth through the entire longitudinal section of the implant (22.1%, Fig. 7b) were obvious when compared to bone ingrowth in the outermost axial section of the implant (14.5%, Fig. 7b) and through a section in contact with the cortex (28.9%, Fig. 7d). While bone was found throughout the implant regardless of location, the extent of bone ingrowth within the implant was highly dependent on its position respective to cortical bone (14.5 vs. 28.9%).

3.4 Spatial quantification of bone response

The use of 3D imaging techniques (Fig. 8) enabled the acquisition of information not available from traditional 2D analysis. Information such as connectivity, smallest pore opening supporting bone progression and bone path along the network of pores were obtained. Using appropriate image analysis tools, it is possible to identify continuous path of mineralized bone matrix inside the porous network. The path of bone ingrowth from the cortex through the open porous network of the implant was determined, isolated and mapped for a 2 mm spicule with numerous projections (Fig. 8c). The path of this continuous bone segment was visualized in 2D (Fig. 8d) to enable the visualization of the smallest diameter of the bone bridge along the path (47 μm) and the smallest opening that bone passed through (60 μm).

In order to study the impact of the porous network interconnectivity on bone ingrowth, successive morphological dilations were performed to gradually close the pore

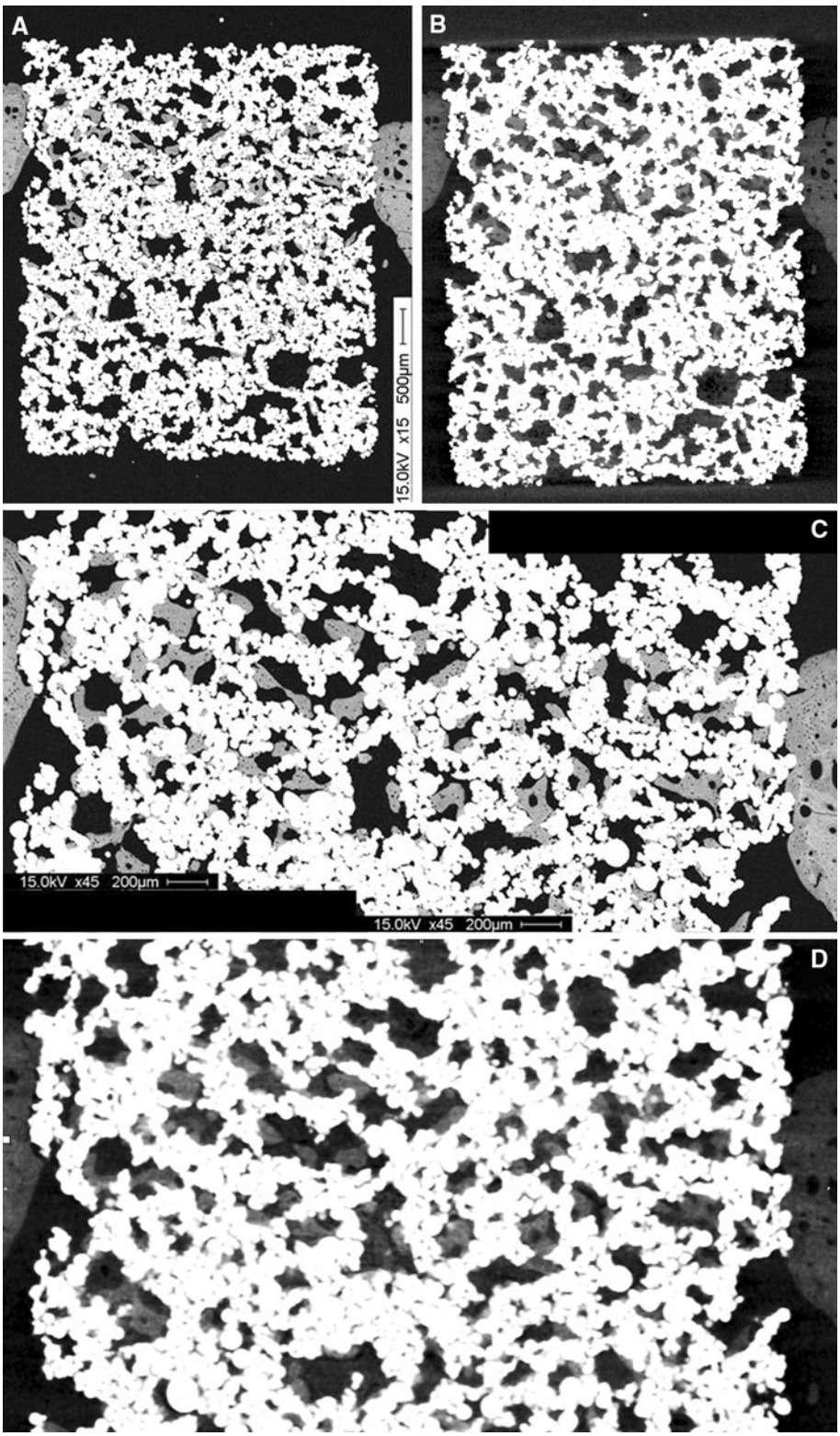

Fig. 5 Direct comparison of the same titanium foam section by BSEM and μCT imaging. **a** low magnification BSEM image and **b** low magnification μCT image. **c** Composite BSEM image at higher power showing ingrowth in the cortical region of the implant. **d** Enlargement of the μCT scan taken at the same location. In all images, titanium foam is *white* and bone is *dark grey*

interconnections. The mineralized bone matrix volume fraction in pores closed by a given level of dilation was then calculated and expressed as a function of the pore interconnect size (Fig. 9). The results show that no bone is present in the pores connected by openings smaller than 9.4 μm. The analysis indicates that these pores represent less than 5.6% of the volume of the implant. Mineralized matrix is observed in the pores connected by openings

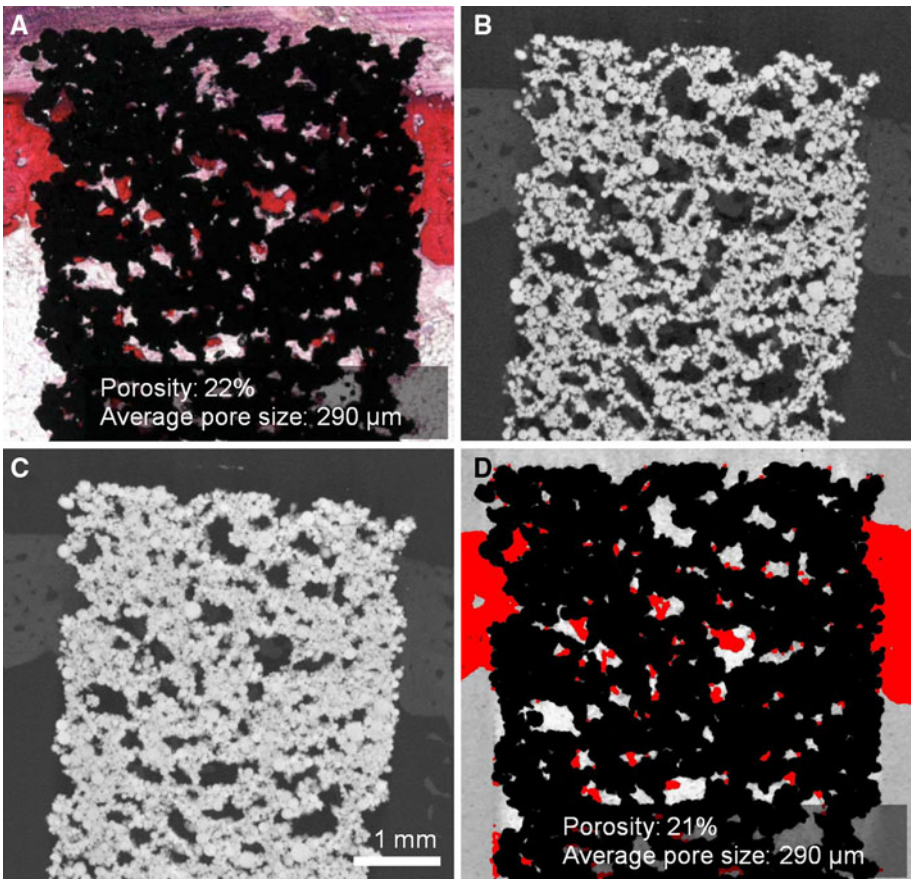

Fig. 6 Comparison of bone ingrowth in light microscopy (LM) and 2D µCT images of the same 85 µm section. **a** LM image of a slice stained with basic fuschin (*red*: bone) and counter stained with methylene blue (soft tissue: *blue*, titanium foam: *black*). **b** 2D µCT longitudinal section reconstructed from a 3.4 µm thick slice at the surface of the same specimen (titanium foam: *light grey*, bone: *dark grey*). **c** 2D µCT longitudinal section reconstructed with the superposition of 3.4 µm thick slices to obtain the complete 85 µm section (titanium foam: *light grey*, bone: *dark grey*). This simulates the projection artifact through a thick LM specimen. **d** Digitally processed image of **c** after segmentation (binarization, inverted lockup table, anisotropic diffusion filtering and contrast enhancement). Titanium in *black* and bone is *red* (Color figure online)

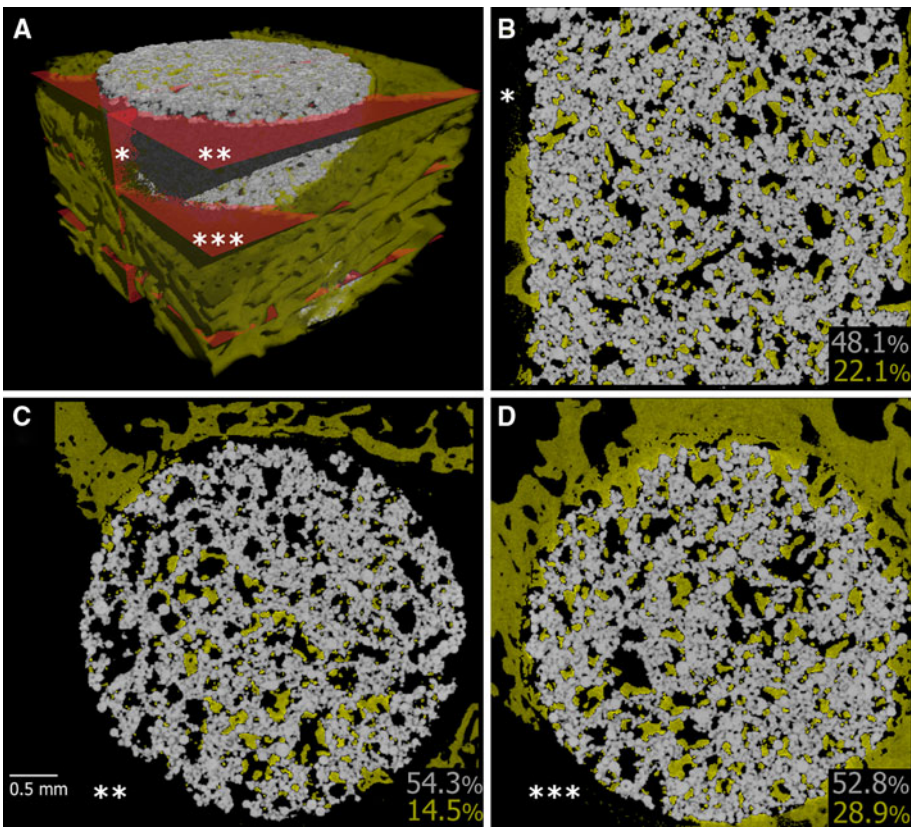

Fig. 7 **a** X-ray µCT 3D reconstruction of the implant (*white*) in the condyle of the distal femur (*light brown*) with the locations of the 2D cross sections presented in **b** longitudinal view, **c** and **d** in axial views. The *asterisk* symbols in each image correspond to the sectioning level and plane in **a**. Titanium is *white* and the bone fraction in pores is *light brown* (Color figure online)

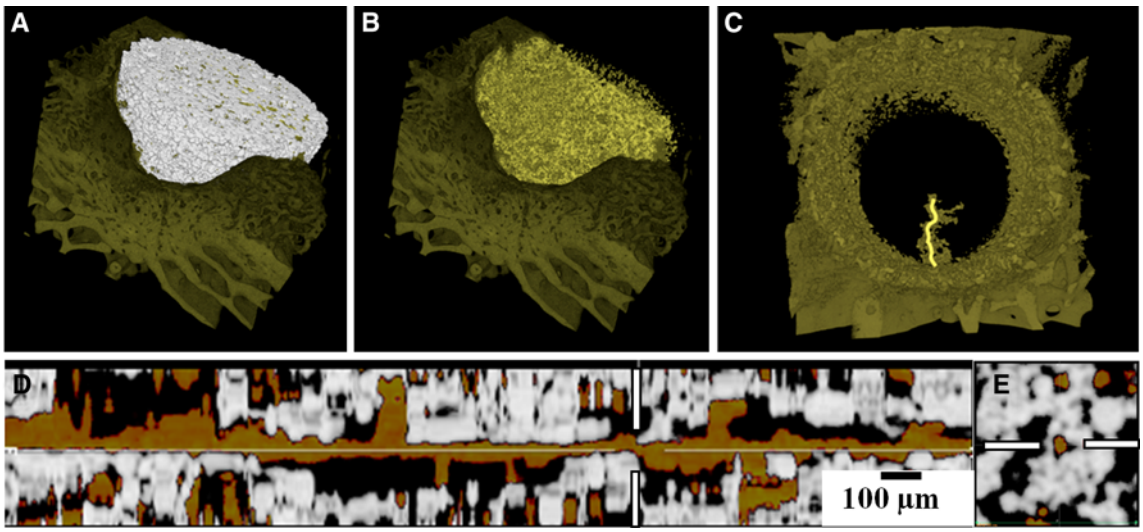

Fig. 8 **A**) 3D µCT reconstruction showing the porous titanium foam implant (*grey*) in the bone (*brown*). **B**) Visualisation of the bone within the titanium foam after digital removal of the titanium implant. **C**) Presentation of one path of bone mineralization into the porous structure of the foam from the region surrounding the implant. **D**) Continuous path of bone mineralized matrix along the line presented in C) after an unwarping transformation (titanium is *grey*, bone is yellow and porosity, non-mineralized tissues and mounting resin are merged in black). **E**) Presentation of a section perpendicular to the bone canal where the smallest bone diameter observed along the canal in D, and indicated by the *white* lines was 47 µm (Color figure online)

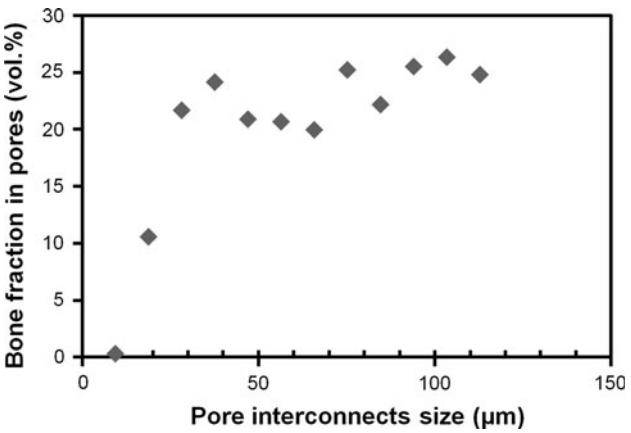

Fig. 9 Bone fraction in the porosity as a function of the interconnect size measured on the full 3D volume of the implant

larger than 18.8 µm. The results also show that when the openings are larger than 28.2 µm, bone density varies between 20 and 25% and is not affected by the size of the openings.

4 Discussion

In this study, µCT was used to quantify bone ingrowth within porous Ti implants. The results were directly compared to those obtained by standard hard tissue histology based techniques (LM and BSEM) on the same sections.

The high resolution µCT imaging of bone within the porous Ti implants obtained in this study was facilitated by the high energy micron-sized X-ray beam, large amorphous-silicon flat panel detector and local threshold technique. Despite the same threshold value, small difference in average porosities measured in 2D and 3D from µCT might be related to the smaller number of samples measured in 2D compared to the thousands of slices for 3D measurements. The significant and relatively large differences in the porosity and pore size between LM and µCT are attributed to projection errors observed in LM. In the LM sections, the image viewed is a projection through the entire volume (85 µm thick) in 2D. As the section thickness increases, an increasing amount of adjacent Ti material that surrounds the pore blocks light transmission. As a result, the porosity was underestimated since material surrounding the pores blocked light and reduced the apparent pore size. This effect is clearly demonstrated when comparing Fig. 6b and c presenting µCT slices of different thicknesses (3.4 and 85 µm thick slices). These images as well as the porosity and pore size measurements agreed well when the µCT image was generated by the addition of 25 slices of 3.4 µm to obtain the same volume as the entire specimen used for LM imaging (Fig. 6c). The end result was a visual reduction in the average pore area which affects the calculated amount of bone ingrowth (bone area/pore area). This artifact can be minimized using thinner sections for LM, ideally 10–20 microns. Thinner sections are, however, more difficult to produce and their fabrication represents technical challenges, especially when materials with different properties, such as Ti and bone, are present. Such artifacts can also be avoided using

BSEM imaging whereby, the back scattered electron signal originates from the first 2.5 μm of the sample surface and, thus, the projection error is prevented. As a result, the implant porosity measured by BSEM is close to that obtained in 2D with μCT (44.0 ± 2.3 vs. 48.4 ± 0.6%).

The difference in sharpness between BSEM and μCT image is mainly due to the ratio between the image resolution (pixel size or image sampling) and the spatial resolution (spot size or physical sampling) which is above unity (pixel size/spot size = 7 μm/2.5 μm = 2.8) for BSEM and below unity (voxel size/spot size = 3.7 μm/4.5 μm = 0.82) for μCT.

Advantageously, μCT also enabled the visualization and quantification of bone in different implant regions and planes which were not available when using standard sectioning techniques. Virtual sectioning of the implant permitted a full use of the information available in the specimens. For example, bone ingrowth in both longitudinal and axial planes could be easily obtained on the same specimens. The location of implant sections was of particular importance as the results of this study indicate that bone ingrowth can vary by as much as 100% depending upon the section location. Bone ingrowth near cortical bone (28.9%) was significantly greater than that in cancellous regions (14.5%) (Fig. 7). Compared to traditional techniques, an important benefit of μCT is the ability to quantify bone formation within the entire implant without introducing potential bias due to the location or orientation of the sectioning plane.

Quantification of intact, embedded specimens also provides a significant research advantage as samples are not destroyed during preparation. As a result, samples remain available for analysis at future dates when new questions, techniques, instruments and analytical approaches become available. Microtomographic analysis also offers significant advantages in terms of the time and effort required for specimen preparation and image acquisition. To take full advantage of the technique, the specimens must be small to get the optimal resolution. This should be obtained by harvesting the implant out of the implantation site.

In addition to the advantages listed above, the μCT/3D analysis generated information that was not available in 2D. For example, bone within the implant could be visualized in 3D, the pore diameters and diameter, length, path and interconnectedness of bone spicules along a path of mineralization inside the implant were presented in this study. The Ti foam used in this study resulted in a range of pore sizes and pore openings. Mineralized tissue was observed within pores connected by openings of 18.8 μm and larger. This value is not the same as the average pore size that is commonly reported in the literature [18]. It is important to note that most studies refer to the pore size rather than the *interconnect size* since interconnect size is difficult to measure in 2D. Pore openings larger than 28.5 μm did not affect bone formation and suggest 28.5 μm may be a minimum opening size for efficient cell migration.

In this work, the choice of the μCT acquisition conditions was mainly driven by the maximization of the spatial resolution and the increase of the signal-to-noise ratio (SNR). The spatial resolution is governed by the microfocus X-ray source power (voltage and current) and, therefore, the power was set to the lowest setting allowing X-ray transmission through the sample and avoiding saturation of the detector. This power setting was, thus, dependent on the specimen size and density (see Table 1). To maximize the SNR, it was found, for the Perkin-Elmer flat panel detector and the X-ray source power used in this study, that a minimum of 8 frames averaging and a minimum of 500 ms integration time were required. Larger number of frames and longer integration time did not result in additional improvement of the SNR. Finally, the beam hardening filter was optimized for the μCT acquisition parameters to obtain an exponential relationship between X-ray absorption (Detected Intensity/Initial Intensity) and X-ray path length in titanium (using a 20° titanium wedge). For the conditions shown in Table 1, only the 0.5 mm Cu filter permitted a relationship matching Beer's law. The selection of these acquisition parameters along with the local threshold method provided conditions to minimize noise even though three material phases (titanium, mineralized bone and soft tissues) with huge electron density difference were present in the specimens.

One of the limitations of μCT was the inability to discriminate non mineralized tissues (fibrous tissues, marrow, and resin). This limitation results from the low X-ray absorption coefficients in these phases. Additional work to increase the contrast between these different phases potentially with the use of contrast agents (X-ray markers) could allow phase differentiation, in a similar way that staining is used in LM to differentiate different biological tissues.

5 Conclusions

Microtomographic analysis is a rapid, suitable and accurate technique for the analysis of bone formation within porous Ti implants. The data and images obtained by μCT were comparable to those obtained by traditional histology-based techniques (LM and BSEM). The μCT approach described in this study is advantageous since it was non-destructive and did not require manual specimen preparation. Since the entire volume of the specimen was scanned, greater accuracy and reduced sampling bias is expected as a benefit. The μCT method also generated data that was not

easily available in 2D, such as the pore and bone connectivity within the implant. The results of this study support the use of μCT as a tool to quantify bone growth into metal implants.

Acknowledgments The authors would like to thanks J.P.Nadeau for the preparation of the specimens and are also grateful for Dr. L Lim's assistance with the animal surgery. The support of the team of Object Research System (ORS) inc. was also greatly appreciated.

References

1. Della Valle CJ, Mesko NW, Quigley L, Rosenberg AG, Jacobs JJ, Galante JO. Primary total hip arthroplasty with a porous-coated acetabular component. J Bone Joint Surg Am. 2009;91(5): 1130–5.
2. Levine BR, Sporera S, Poggie RA, Della Vallea CJ, Jacobs JJ. Experimental and clinical performance of porous tantalum in orthopedic surgery. Biomaterials. 2006;27(27):4671–81.
3. Sporer S, Paprosky WG. The use of a trabecular metal acetabular component and trabecular metal augment for severe acetabular defects. J Arthroplasty. 2006;21(6-suppl):83–6.
4. Ryan G, Pandit A, Apatsidis DP. Fabrication methods of porous metals for use in orthopaedic applications. Biomaterials. 2006; 27(13):2651–70.
5. Lefebvre LP, Baril E, Bureau MN. Effect of the oxygen content in solution on the static and cyclic deformation of titanium foams. J Mater Sci: Mater Med. 2009;20(11):2223–33.
6. Zhang Y, Ahn PB, Fitzpatrick DC, Heiner AD, Poggie RA, Brown TD. Interfacial frictional behavior: cancellous bone, cortical bone, and a novel porous tantalum biomaterial. J Musculoskeletal Res. 1999;3(4):245–51.
7. Heiner AD, Brown TD. Frictional coefficients of a new bone ingrowth structure. Trans Orthopaed Res Soc. 2007;32:1623.
8. Boyde A, Jones SJ. Back-scattered electron imaging of skeletal tissues. Metab Bone Dis Relat Res 1983–1984;5(3):145–50.
9. Assad M, Jarzem P, Leroux MA, Couillard C, Chernyshov AV, Charrette S, Rivard CH. Porous titanium-nickel for intervertebral fusion in a sheep model: part 1. Histomorphometric and radiological analyses. J Biomed Mater Res B Appl Biomater. 2003; 64B(2):107–20.
10. Odgaard A, Gundersen HJG. Quantification of connectivity in cancellous bone, with special emphasis on 3-D reconstruction. Bone. 1993;14(2):173–82.
11. Feldkamp LA, Goldstein SA, Parfitt M, Jesion G, Kleerekoper M. The direct examination of three-dimensional bone architecture in vitro by computed tomography. J Bone Miner Res. 1989;4(1): 3–11.
12. Bouxsein ML, Boyd SK, Christiansen BA, Guldberg RE, Jepsen KJ, Müller R. Guidelines for assessment of bone microstructure in rodents using micro-computed tomography. J Bone Miner Res. 2010;25(7):1468–86.
13. Gebauer M, Barvencik F, Mumme M, Beil FT, Vettorazzi E, Rueger JM, et al. Microarchitecture of the radial head and its changes in aging. Calcif Tissue Int. 2010;86(1):14–22.
14. Zhang ZM, Li ZC, Jiang LS, Jiang SD, Dai LY. Micro-CT and mechanical evaluation of subchondral trabecular bone structure between postmenopausal women with osteoarthritis and osteoporosis. Osteoporos Int. 2009;21(8):1383–90.
15. Bonse U, Busch F, Günnewig O, Beckmann F, Pahl R, Delling G, et al. 3D computed X-ray tomography of human cancellous bone at 8 microns spatial and 10(-4) energy resolution. Bone Miner. 1994;25(1):25–38.
16. Kirby BJ, Davis JR, Grant JA, Morgan MJ. Monochromatic microtomographic imaging of osteoporotic bone. Phys Med Biol. 1997;42(7):1375–85.
17. Bernhardt R, Scharnweber D, Müller B, Thurner P, Schliephake H, Wyss P, et al. Comparison of microfocus and synchrotron X-ray tomography for the analysis of osseontegration around Ti6Al4 V-implants. Euro Cell Mater. 2004;7:42–51.
18. Bobyn JD, Pilliar RM, Cameron HU, Weatherly GC. The optimum pore size, for the fixation of porous-surfaced metal implants by the ingrowth of bone. Clin Orthop Relat Res. 1980;150: 263–70.
19. Baril E, Lefebvre LP, Piché N. X-ray microtomographic visualization and quantification of metallic foam structure filled with second phases—examples in biomedical applications. The proceeding of the 6th Int. Conf on Porous Metals and Metallic Foams (Metfoam 2009); 2009 Sep 1–4; Bratislava, Slovakia.
20. Otsuki B, Takemoto M, Fujibayashi S, Neo M, Kokubob T, Nakamura T. Pore throat size and connectivity determine bone and tissue ingrowth into porous implants: three-dimensional micro-CT based structural analyses of porous bioactive titanium implants. Biomaterials. 2006;27(35):5892–900.
21. Jones AC, Arns CH, Sheppard AP, Hutmacher DW, Milthorpe K, Knacksted MA. Assessment of bone ingrowth into porous biomaterials using MICRO-CT. Biomaterials. 2007;28(15):2491–504.
22. Lefebvre LP, Thomas Y. Method of making open cell material. US Patent No. 6,660,224 B2, 2003.
23. Wazen R, Lefebvre LP, Baril E, Nanci A. Initial evaluation of bone ingrowth into a novel porous titanium coating. J Biomed Mat Res-Part B. 2010;94(1):64–71.
24. Gauthier M, Menini R, Bureau MN, So SKV, Dion MJ, Lefebvre LP. Properties of novel titanium foams intended for biomedical applications. ASM Materials and Processes for Medical Devices Conference, 2003 Sep 8–10; Anaheim, California: 382–387.
25. Hacking SA, Bobyn JD, Tanzer M, Krygier JJ. The osseous response to corundum blasted implant surfaces in a canine hip model. Clin Orthop. 1999;364:240–53.
26. Hacking SA, Harvey EJ, Tanzer M, Bobyn JD, Krygier JJ. Acid etched microtexture for enhancement of bone growth into porous coated implants. J Bone Joint Surg. 2003;85(8):1182–9.
27. Habibovic P, de Groot K. Osteoinductive biomaterials—properties and relevance in bone repair. J Tissue Eng Regen Med. 2007;1(1):25–32.
28. Hsieh J. Computed tomography: principles, design, artifacts, and recent advances. 2nd ed. Bellingham, New York: SPIE Press and Wiley; 2009.
29. Sethian JA. Level set methods and fast marching methods : evolving interfaces in computational geometry, fluid mechanics, computer vision, and materials science. 2nd ed. Cambridge: Cambridge University Press; 1999.